Current-driven dynamics of Dzyaloshinskii domain walls in the presence of in-plane fields: Full micromagnetic and one-dimensional analysis

Eduardo Martinez, Satoru Emori, Noel Perez, Luis Torres, and Geoffrey S. D. Beach

Articles you may be interested in

Chiral magnetization textures stabilized by the Dzyaloshinskii-Moriya interaction during spin-orbit torque switching
Appl. Phys. Lett. 104, 092403 (2014); 10.1063/1.4867199

Interlayer exchange coupled composite free layer for CoFeB/MgO based perpendicular magnetic tunnel junctions
J. Appl. Phys. 114, 203901 (2013); 10.1063/1.4833252

Stability analysis of current-driven domain wall in the presence of spin Hall effect
J. Appl. Phys. 114, 093912 (2013); 10.1063/1.4820767

Current-driven domain wall motion along high perpendicular anisotropy multilayers: The role of the Rashba field, the spin Hall effect, and the Dzyaloshinskii-Moriya interaction
Appl. Phys. Lett. 103, 072406 (2013); 10.1063/1.4818723

Optimization of Co/Pt multilayers for applications of current-driven domain wall propagation
J. Appl. Phys. 110, 083913 (2011); 10.1063/1.3654045

Current-driven dynamics of Dzyaloshinskii domain walls in the presence of in-plane fields: Full micromagnetic and one-dimensional analysis

Eduardo Martinez,[1,a)] Satoru Emori,[2] Noel Perez,[1] Luis Torres,[1] and Geoffrey S. D. Beach[2]

[1]*Universidad de Salamanca, Plaza de los Caidos s/n, E-37008 Salamanca, Spain*
[2]*Massachusetts Institute of Technology, Cambridge, Massachusetts 02139, USA*

Current-induced domain wall motion along high perpendicular magnetocrystalline anisotropy multilayers is studied by means of full micromagnetic simulations and a one-dimensional model in the presence of in-plane fields. We consider domain wall motion driven by the spin Hall effect in the presence of the Dzyaloshinskii-Moriya interaction (DMI). In the case of relatively weak DMI, the wall propagates without significant tilting of the wall plane, and the full micromagnetic results are quantitatively reproduced by a simple rigid one-dimensional model. By contrast, significant wall-plane tilting is observed in the case of strong DMI, and a one-dimensional description including the wall tilting is required to qualitatively describe the micromagnetic results. However, in this strong-DMI case, the one-dimensional model exhibits significant quantitative discrepancies from the full micromagnetic results, in particular, when high longitudinal fields are applied in the direction of the internal domain wall magnetization. It is also shown that, even under thermal fluctuations and edge roughness, the domain wall develops a net tilting angle during its current-induced motion along samples with strong DMI. © 2014 AIP Publishing LLC. [http://dx.doi.org/10.1063/1.4881778]

I. INTRODUCTION

Recent experiments[1–8] have demonstrated that current-induced domain wall motion (CIDWM) in high perpendicular magnetocrystalline anisotropy (PMA) multilayers consisting of an ultrathin ferromagnet (Co, CoFe, or CoFeB) sandwiched between a heavy-metal (Pt or Ta) and an insulator (AlO, MgO, or TaN), is anomalously efficient, exhibiting large effective fields ($\gg 10 Oe/(10^{11}A/m^2)$) and reaching high velocities ($\sim 400\,m/s$). These results are very promising for future development of domain wall-based nanodevices,[9] but at the same time, they have also opened new fundamental questions on the underlying physics. It was initially suggested[5] that such a large efficiency could be due to the lack of inversion symmetry of the dissimilar non-magnetic layers sandwiching the ferromagnetic layer and that this asymmetry would induce a Rashba spin-orbit interaction at the interfaces,[10–15] which could support the standard non-adiabatic spin transfer torque (STT).[16,17] The effective field from the Rashba effect is proportional to the applied current density flowing through the multilayer ($\vec{j}_a = j_a \vec{u}_x$), the spin polarization factor of the current (P) and the Rashba parameter (α_R), which was initially estimated[5,11,18] to be around $\alpha_R \approx 10^{-10} eVm$. The direction of the Rashba field is perpendicular to both the $\vec{j}_a$ and to the direction of the stack inversion asymmetry ($\vec{u}_z$). However, apart from the strong Rashba parameter required to explain the high efficiency, the domain wall (DW) motion was along the current, an observation which is contrary to the standard STT,[16,17] and either a negative non-adiabatic parameter ($\xi < 0$) or a negative polarization factor ($P < 0$) was required for this explanation to be consistent with the experimental measurements.[5]

Two years after the pioneering work by Miron *et al.*,[5] Haazen and co-workers[6] presented a study of the CIDWM along Pt/Co/Pt multilayer strips. Due to the nominally identical Pt/Co and Co/Pt interfaces in this system, the interfacial Rashba effect is expected to be negligible. It was also confirmed that the standard STT alone could not drive the walls,[19–21] consistent with a very low spin polarization of these systems, as also reported in other experimental studies.[21–23] The results by Haazen *et al.*[6] indicate that in the absence of longitudinal field, the DWs adopt a Bloch configuration,[24] which cannot be displaced by the spin Hall effect (SHE)[25] because the internal DW magnetization is parallel to the polarization of the SHE current from the thicker Pt layer ($\pm\vec{u}_y$). Indeed, the CIDWM in Ref. 6 was only detected under the presence of an in-plane longitudinal magnetic field B_x along the strip axis, parallel to the injected current $\vec{j}_a$. This field rotates the internal DW magnetization from the transverse direction (y-axis) to the longitudinal direction (x-axis), suggesting that the net SHE[26–32] from the heavy-metal Pt layers exerts a torque on the DW moment $\vec{m}_{DW}$ in a manner similar to a perpendicular magnetic field ($\pm B_z\vec{u}_z$), thereby resulting in CIDWM.

More recently, the CIDWM was experimentally studied in Ref. 7 for an ultrathin CoFe on top of two different heavy-metals layers (Pt or Ta). Contrary to the case studied by Haazen *et al.*,[6] DW motion was achieved even in the absence of the longitudinal fields for both Ta/CoFe and Pt/CoFe. The DW moved along the current in the Pt-sample and along the electron flow in the Ta-sample, in agreement with the SHE effective field picture and the opposite signs of the spin Hall angles for Pt and Ta.[29,30] These observations were found

---

a)Author to whom correspondence should be addressed. Electronic mail: edumartinez@usal.es

consistent with the prediction by Thiaville *et al.*,[33] where it was suggested that the anisotropic interfacial Dzyaloshinskii-Moriya exchange interaction (DMI)[34–39] at the heavy-metal/ferromagnet interface imposes a Neel DW configuration ($\vec{m}_{DW} \approx \pm \vec{u}_x$) with a fixed chirality, instead of the Bloch configuration ($\vec{m}_{DW} \approx \pm \vec{u}_y$) expected from magnetostatics. In contrast to the dominant ferromagnetic interaction, which favours collinear alignment of neighboring spins, the DMI prefers an orthogonal orientation with a given chirality.[34–39] In both the Pt and Ta samples studied in Ref. 7, the DWs exhibit Neel configuration with left-handed chirality at rest. Alternate up-down and down-up walls in a strip can be displaced by the SHE unidirectionally, along conventional current in the Pt sample and along electron flow in the Ta sample. Similar interpretation of their corresponding experiments was also given by Ryu *et al.*,[8] which was also consistent with the DMI-SHE scenario: the interfacial DMI stabilizes Neel walls with a given chirality, and they are then driven by the SHE. Note that other recent work also indicates the essential role of both the DMI and the SHE on describing the switching processes in similar PMA multilayers.[40]

Except for a few cases,[33,41,42] most of the experiments on the CIDWM in these PMA multilayers are interpreted in terms of a simple one-dimensional model (1DM). However, a detailed micromagnetic analysis, considering the full spatial dependence of the magnetization, is needed to evaluate the validity of simple 1D models for various experimental systems (weak and strong DMI, positive and negative spin Hall angles, pinning, etc.) and to understand quantitatively the CIDWM by the SHE along multilayers with DMI in the presence of in-plane fields. Application of in-plane fields is also essential to quantify the magnitude of the DMI (D). In the present work, a full micromagnetic study of the CIDWM along samples with DMI is presented with emphasis on the influence of in-plane fields. Section II introduces the details of the micromagnetic model (μM) incorporating both the SHE and DMI, and also typical results for both typical low- and high-DMI samples. The 1DM is described in Sec. III and the comparison of the results predicted by the μM and 1D models is given in Sec. IV. Also in Sec. IV, the CIDWM is studied under realistic conditions including edge roughness and thermal effects. The conclusions of this study are presented in Sec. V.

II. MICROMAGNETIC MODEL

A. Material parameters and micromagnetic model details

We consider a thin ferromagnetic CoFe strip with a cross section of $L_y \times L_z = 160 \, nm \times 0.6 \, nm$ on top of a heavy metal layer of Ta or Pt. Based on experimental magnetometry,[43] the following common parameters for both the Ta/CoFe and Pt/CoFe samples were considered: saturation magnetization $M_s = 7 \times 10^5$ A/m, exchange constant $A = 10^{-11}$ J/m, and uniaxial anisotropy constant $K_u = 4.8 \times 10^5$ J/m^3. The specific parameters for the Ta-sample (Ta/CoFe/MgO)[43] are a weak DMI parameter $D = -0.05$ mJ/m^2, a high negative spin Hall angle $\theta_{SH} = -0.11$, and a low Gilbert damping $\alpha = 0.03$ (see Refs.

44 and 45). On the other hand, the values to model the Pt-sample (Pt/CoFe/MgO)[43] are a strong DMI parameter $D = -1.2$ mJ/m^2, a positive spin Hall angle $\theta_{SH} = +0.07$, and a high Gilbert damping $\alpha = 0.3$ (see Ref. 46).

For both the Ta and Pt samples, the amplitude of the DMI ($|D|$) is high enough to overcome shape anisotropy, and therefore, the DWs adopt a Neel equilibrium configuration. For the negative value of the DMI ($D < 0$), these Neel walls depict a left-handed chirality with two possible configurations: (a) up-down with internal DW magnetization $\vec{m}_{DW}$ pointing along the negative x-axis ($\vec{m}_{DW} \approx -\vec{u}_x$) or (b) down-up with internal DW magnetization along the positive x-axis ($\vec{m}_{DW} \approx +\vec{u}_x$). These configurations are shown in Figs. 1(a) and 1(b), respectively. In what follows, we restrict our discussion to the left-handed up-down wall, but the results for the down-up case can be straightforwardly deduced by symmetry arguments.

Under injection of a spatially uniform current density along the x-axis $\vec{j}_a = j_a \vec{u}_x$, the magnetization dynamics is governed by the augmented Landau-Lifshitz Gilbert (LLG) equation

$$\frac{d\vec{m}}{dt} = -\gamma_0 \vec{m} \times \vec{H}_{eff} + \alpha \left(\vec{m} \times \frac{d\vec{m}}{dt} \right) + \vec{\tau}_{ST} + \vec{\tau}_{SO}, \quad (1)$$

where $\vec{m}(\vec{r}, t) = \vec{M}(\vec{r}, t)/M_s$ is the normalized local magnetization, γ_0 is the gyromagnetic ratio, and α the Gilbert damping parameter. $\vec{H}_{eff}$ is effective field derived from the energy density of the system ($\vec{H}_{eff} = -\frac{1}{\mu_0 M_s} \frac{\delta \epsilon}{\delta \vec{m}}$), which apart from the standard exchange, magnetostatic, uniaxial anisotropy, and Zeeman contributions also includes the anisotropic exchange DMI.[34–36] In the thin-film approach ($L_z \ll L_y, L_x$), the interfacial DMI energy density ϵ_{DM} is given by[33,36,48]

$$\epsilon_{DM} = -D[m_z \nabla \cdot \vec{m} - (\vec{m} \cdot \nabla)m_z], \quad (2)$$

where D is the DMI parameter describing its intensity. The DMI effective field $\vec{H}_{DM}$ is therefore

$$\vec{H}_{DM} = -\frac{2D}{\mu_0 M_s} \left[\frac{\partial m_z}{\partial x} \vec{u}_x + \frac{\partial m_z}{\partial y} \vec{u}_y - \left(\frac{\partial m_x}{\partial x} + \frac{\partial m_y}{\partial y} \right) \vec{u}_z \right]. \quad (3)$$

In the absence of DMI ($D = 0$), the exchange interaction imposes boundary conditions at the surfaces of the sample[47]
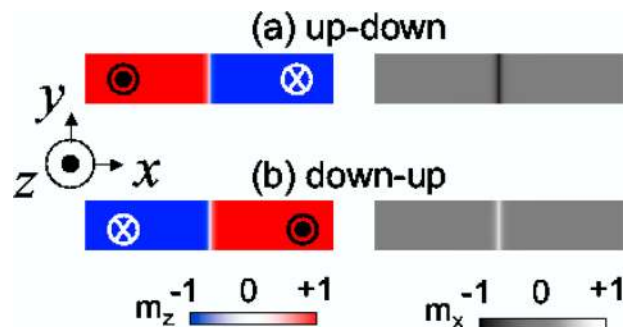

FIG. 1. Micromagnetic snapshots of left-handed ($D < 0$) walls at rest: (a) up-down and (b) down-up configurations.

such that the magnetization vector does not change along the surface ($\partial \vec{m}/\partial n = 0$, where $\partial/\partial n$ indicates the derivative in the outside direction normal to the surface of the sample). However, in the presence of the interfacial DMI, this boundary condition has to be replaced by[48]

$$\frac{\partial \vec{m}}{\partial n} = \frac{D}{2A} \vec{m} \times (\vec{n} \times \vec{u}_z), \tag{4}$$

where $\vec{n}$ represents the local unit vector normal to each sample surface. The spin-transfer torque (STT) $\vec{\tau}_{ST}$ is given by[16,17]

$$\vec{\tau}_{ST} = b_J (\vec{u}_x \cdot \nabla) \vec{m} - \xi b_J \vec{m} \times (\vec{u}_x \cdot \nabla) \vec{m}, \tag{5}$$

where the STT coefficient is $b_J = j_a \frac{\mu_B P}{e M_s}$ with μ_B the Bohr magneton and $e < 0$ the electron's charge. P is the spin polarization factor and ξ the dimensionless non-adiabatic parameter.

Finally, $\vec{\tau}_{SO}$ describes the spin-orbit torques (SOTs)

$$\vec{\tau}_{SO} = -\gamma_0 \vec{m} \times \vec{H}_R + \eta \gamma_0 \xi \vec{m} \times (\vec{m} \times \vec{H}_R)$$
$$- \gamma_0 \vec{m} \times (\vec{m} \times H_{SH} \vec{u}_y), \tag{6}$$

where two contributions from the Rashba effect (1st and 2nd terms in (6)) and one from the spin Hall effect (3rd term in (6)) can be identified. In the presence of the Rashba interaction, the charge current in the thin ferromagnetic layer flowing parallel to the asymmetric interfaces generates a spin accumulation that can interact with the local magnetization via an exchange coupling, mediated by a Rashba effective field $\vec{H}_R = H_R \vec{u}_y$ given by[5,11,12]

$$\vec{H}_R = \frac{\alpha_R P}{\mu_0 \mu_B M_s} (\vec{u}_z \times \vec{j}_a) = \frac{\alpha_R P j_a}{\mu_0 \mu_B M_s} \vec{u}_y, \tag{7}$$

with α_R being the Rashba parameter. Another Rashba SOT could also arise either from the spin diffusion inside the magnetic layer or from a spin current associated with the Rashba interaction at the interfaces with the spin-orbit metal.[14] These phenomena have been predicted to contribute to the SOT by means of an additional non-adiabatic contribution to the Rashba SOT,[13,14] which is proportional to the non-adiabatic parameter ξ (2nd term in (6)). Another possible source of SOT originates from the SHE[26,27] where spin-dependent scattering of an in-plane charge current in a heavy metal (e.g., Ta and Pt) generates an out-of-plane spin current. This spin current can be injected into the ferromagnetic layer, resulting in an additional SOT (3rd term in (6)), where the amplitude of the SHE effective field H_{SH} is given by[29–32]

$$H_{SH} = \frac{\hbar \theta_{SH} j_a}{\mu_0 2 e M_s L_z} = \frac{\mu_B \theta_{SH} j_a}{\gamma_0 e M_s L_z}, \tag{8}$$

where L_z is the thickness of the ferromagnetic layer. θ_{SH} is the Spin Hall angle, which is defined as the ratio between the spin and charge current densities. Here, we assume that the SHE generates a Slonczewski-like torque only given by the 3rd term in (6), although recent experiments suggest that the

SHE could also potentially generate a field-like torque[49–51] with the same symmetry as the 1st term in (6).

Several experiments[7,8,40,43] indicate that the main ingredients to explain the current-driven DW motion in these multilayers are the DMI and SHE, and nowadays a relatively general consensus has been reached in this interpretation: the DMI stabilizes a Neel configuration with a given chirality and the SHE is the main mechanism for driving these chiral DWs along these PMA multilayers.[7,8,42] A theoretical analysis of different combinations of STT, Rashba, SHE, and DMI compared with the experimental results[5] was discussed in Refs. 52 and 53, which also supports the DMI and SHE scenario. Therefore, the micromagnetic (μM) results described hereafter were obtained by solving the LLG Eq. (1) in the absence of STT ($P = 0$) and Rashba ($\alpha_R = 0$) contributions. Samples with $L_x = 2.8\,\mu$m in length were discretized in 2D with cells of $\Delta x = \Delta y = 4$ nm in side, and thickness equal to the ferromagnetic strip ($L_z = 0.6$ nm). Equation (1) was numerically solved with a 6th-order Runge-Kutta scheme with a time step of 0.1 ps by using GPMagnet, a commercial parallelized finite-difference micromagnetic solver.[54,55] Several tests were performed with cell sizes of 1 nm confirming that similar micromagnetic results are obtained.

B. Micromagnetic results: Temporal evolution of the DW position

We first address CIDWM driven by relatively low current densities, considering weak and strong DMI. Typical micromagnetic (μM) results for the CIDWM ($j_a = +0.1 \times 10^{12}$ A/m^2) along the Ta sample under longitudinal fields (B_x) are depicted in Fig. 2(a) for the up−down configuration. This Ta sample is representative of a weak DMI ($D = -0.05$ mJ/m^2) system with negative spin Hall angle ($\theta_{SH} = -0.11$). Although the DMI is relatively low, it is still high enough to promote Neel walls with left-handed ($D < 0$) chirality at rest. As observed experimentally,[7,43] when a small positive current is applied in the absence of in-plane fields, both up-down and down-up walls propagate along the electron flow (with negative velocity, i.e., along $-\vec{u}_x$) as expected due to the negative spin Hall angle of the
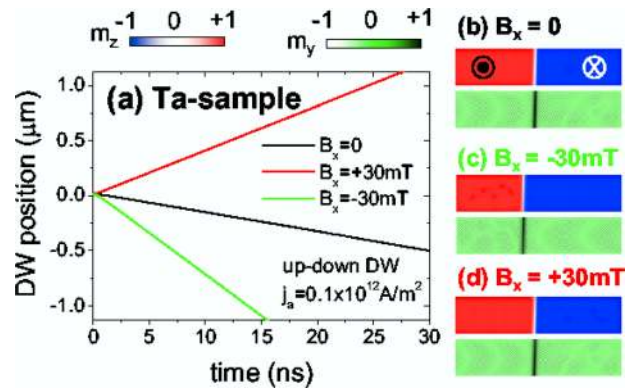

FIG. 2. (a) Micromagnetic results depicting the temporal evolution of the DW position for the Ta-sample ($D = -0.05$ mJ/m^2, $\theta_{SH} = -0.11$, $\alpha = 0.03$) under a current density of $j_a = 0.1 \times 10^{12}$ A/m^2 in the presence of in-plane longitudinal fields. The corresponding steady-state DW configurations are shown in (b) $B_x = 0$, (c) $B_x = +30$ mT, and (d) $B_x = -30$ mT. All results correspond to an up-down configuration.
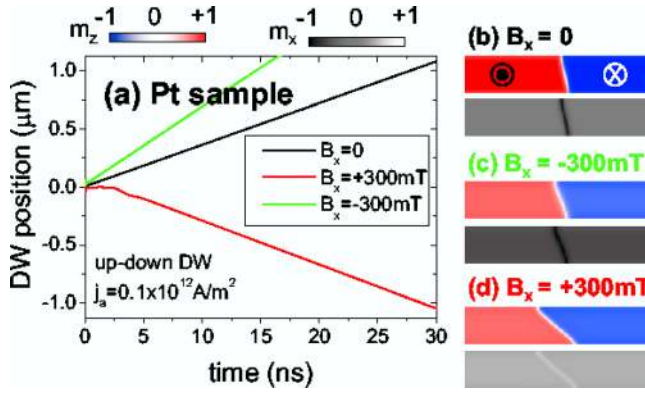
FIG. 3. (a) Micromagnetic results depicting the temporal evolution of the DW position for the Pt-sample ($D = -1.2$ mJ/m^2, $\theta_{SH} = +0.07$, $\alpha = 0.3$) under a current density of $j_a = 0.1 \times 10^{12}$ A/m^2 in the presence of in-plane longitudinal fields. The corresponding steady-state DW configurations are shown in (b) $B_x = 0$, (c) $B_x = +300$ mT, and (d) $B_x = -300$ mT. All results correspond to an up-down configuration.

Ta. For the positive current evaluated in Fig. 2 ($j_a = 0.1 \times 10^{12}$ A/m^2) and zero in-plane field ($B_x = B_y = 0$), the DW reaches a steady-state regime with internal DW magnetization pointing mainly along the $+y$ direction (see Fig. 2(b)). This quasi-Bloch configuration (with internal DW moment given by $\vec{m}_{DW} = m_{DW,x}\vec{u}_x + m_{DW,y}\vec{u}_y$ with $|m_{DW,x}| \ll |m_{DW,y}|$) is also achieved under relatively small positive and negative longitudinal ($B_x \neq 0$) fields (see Figs. 2(c) and 2(d) for $B_x = -30$ mT and $B_x = +30$ mT), but the direction of the DW motion reverses (velocity along $+\vec{u}_x$) for the positive field $B_x = +30$ mT.

As it is shown in Fig. 3 for the same current ($j_a = 0.1 \times 10^{12}$ A/m^2), the μM results are significantly different for the Pt sample, which is archetypal of a strong DMI system ($D = -1.2$ mJ/m^2) with positive spin Hall angle ($\theta_{SH} = +0.07$). Now the DW moves along the current (with positive velocity, i.e., along $+\vec{u}_x$ in the absence of the longitudinal field ($B_x = 0$), and the DW speed increases under high negative longitudinal fields ($B_x = -300$ mT). Under a very high positive field ($B_x = +300$ mT), the DW motion is along the electron flow (against the current, with velocity along $-\vec{u}_x$). Contrary to the behavior of the Ta sample, the internal DW magnetization ($\vec{m}_{DW}$) points mainly along the x-axis: $\vec{m}_{DW} \approx -\vec{u}_x$ for $B_x = 0$ and $B_x = -300$ mT (see Figs. 3(b) and 3(d), respectively), whereas $\vec{m}_{DW} \approx +\vec{u}_x$ for $B_x = +300$ mT as is shown in Fig. 3(c). Also differently from the Ta results, the DW steady states under finite current j_a in the Pt sample exhibit significant tilting, that is, a rotation of the DW normal ($\vec{n}_{DW}$) with respect to the x-axis, which is enhanced by application of the in-plane fields. Note that current-driven DW tilting was also experimentally observed[56] in other systems. The origin of this behavior derives from the fact that DMI tends to maintain $\vec{m}_{DW}$ parallel to $\vec{n}_{DW}$. When a torque is applied that cants $\vec{m}_{DW}$ away from $\vec{u}_x$, strong DMI causes the DW to tilt in order to minimize the angle between $\vec{n}_{DW}$ and $\vec{m}_{DW}$. Although there is an associated energy cost due to the increased DW length, the net energy should be lowered by DW tilting if the DMI is sufficiently strong.[42,43] For clarity, the physical description of these dynamical behaviors and the explanation of these micromagnetic results for both the Ta

and the Pt samples will be discussed after introducing the one-dimensional model in Sec. III.

III. ONE-DIMENSIONAL MODEL

The 1DM is a useful tool to describe the former micromagnetic results and to interpret experimental results. Since its initial introduction by Walker and Slonczewski,[57,58] several authors have made contributions to include the STTs,[16,17] the SOTs,[32,41,52,53,59–62] the DMI,[7,33,41] as well as pinning[63–65] and thermal effects.[66–68] The most recent contribution was made by Boulle *et al.*[42] where the DW tilting was included as an additional degree of freedom to analyze and describe the experimental observations[56] of the dynamics of Dzyaloshinskii walls in the presence of the transverse fields (B_y). Here, we adapt this collective coordinate model (here after, Tilt-1DM) and extend it to also analyze the influence of the longitudinal fields (B_x) on the DW dynamics. In the framework of this Tilt-1DM, the DW dynamics is described by three coupled differential equations in terms of three time-dependent variables: the DW position $X = X(t)$ along the strip axis (x-axis), the DW angle $\Phi = \Phi(t)$, which is defined as the in-plane (x-y) angle of the internal DW magnetization ($\vec{m}_{DW}$) with respect to the positive x-axis ($\Phi(0) = 0°, 180°$ for Neel DW, and $\Phi(0) = 90°, 270°$ for Bloch DW configurations), and the tilting angle $\chi = \chi(t)$ defined as the angle of the DW normal ($\vec{n}_{DW}$) plane with respect the x-axis (see Fig. 4). These three coupled equations are

$$(1 + \alpha^2)\dot{X} = \frac{\Delta}{\cos\chi}(\Omega_A + \alpha\Omega_B), \quad (9)$$

$$(1 + \alpha^2)\dot{\Phi} = -\alpha\Omega_A + \Omega_B, \quad (10)$$

$$\dot{\chi} = \frac{\left(\dfrac{6\gamma_0}{\alpha\mu_0 M_s \Delta\pi^2}\right)}{\tan^2\chi + \left(\dfrac{L_y}{\pi\Delta\cos\chi}\right)^2}[-\sigma\sin\chi$$
$$+ \pi DQ\sin(\Phi - \chi) - \mu_0 H_K M_s \Delta\sin[2(\Phi - \chi)]], \quad (11)$$

where Ω_A and Ω_B have units of frequency and are given by

$$\Omega_A = -\frac{1}{2}\gamma_0 H_K \sin[2(\Phi - \chi)] - \frac{\pi}{2}\gamma_0 H_y \cos\Phi$$
$$+ \frac{\pi}{2}\gamma_0 H_x \sin\Phi + \frac{\pi}{2}\gamma_0 H_D Q\sin(\Phi - \chi) \quad (12)$$
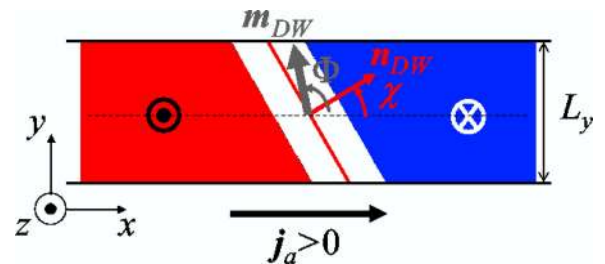$$- \frac{\pi}{2}\gamma_0 H_R \cos\Phi + \frac{b_J}{\Delta}\cos\chi,$$

FIG. 4. Schematic representation of the DW angles considered in the Tilt-1DM: Φ represents the angle of internal DW magnetization $\vec{m}_{DW}$, whereas χ is the angle of the DW normal plane. Both are defined with respect to the positive x-axis.

$$\Omega_B = \gamma_0 QH + \frac{\pi}{2}\gamma_0 QH_{SH}\cos\Phi$$
$$-\xi\frac{\pi}{2}\gamma_0 H_R\cos\Phi + \xi\frac{b_J}{\Delta}\cos\chi, \tag{13}$$

and the DW energy density σ is

$$\sigma = \frac{1}{\cos\chi}[4\sqrt{AK_u} - Q\pi D\cos(\Phi - \chi)$$
$$+\mu_0 H_K M_s\Delta\cos^2[2(\Phi - \chi)] - \pi\mu_0 M_s\Delta H_R\sin\Phi$$
$$-\pi\mu_0 M_s\Delta H_y\sin\Phi - \pi\mu_0 M_s\Delta H_x\cos\Phi]. \tag{14}$$

Here, Q is $+1$ or -1 for up-down and down-up DW configurations. Positive current $(j_a > 0)$ is along the positive x-axis. Δ is the DW width and H_K is the shape anisotropy field $H_K = N_x M_s$, with N_x the magnetostatic factor given by[69] $N_x = L_z Log(2)/(\pi\Delta) \approx 0.0174$. The DW width is estimated to be $\Delta = \sqrt{A/K_{eff}} \approx 7.62$nm, where $K_{eff} = K_u - \mu_0 M_s^2/2$. In the 1D framework, the DMI generates an effective field along the x-axis inside the DW $\vec{H}_D = H_D\vec{u}_x$, which amplitude is given by $H_D = D/(\mu_0 M_s\Delta)$.[33] The applied field has Cartesian components (H_x, H_y, H_z). The total field $H = H_z + H_p(X) + H_{th}(t)$ includes: (i) the applied magnetic field along the easy z-axis (H_z), (ii) the spatial dependent pinning field $(H_p(X))$, which accounts for local imperfections and can be derived from an effective spatial-dependent pinning potential[41,64,67,68] $V_{pin}(X)$ as $H_p(X) = -\frac{1}{2\mu_0 M_s L_y L_z}\frac{\partial V_{pin}(X)}{\partial X}$, and (iii) the thermal field $(H_{th}(t))$, which describes the effect of thermal fluctuations,[67,68] and is assumed to be a random Gaussian-distributed stochastic process with zero mean value $(\langle H_{th}(t)\rangle = 0)$ and uncorrelated in time $(\langle H_{th}(t)H_{th}(t')\rangle = \frac{2\alpha K_B T}{\mu_0\gamma_0 M_s\Delta L_y L_z}\delta(t - t')$, where K_B is the Boltzmann constant and T the temperature). Unless otherwise specified, perfect samples $(H_p(X) = 0)$ at zero temperature $(H_{th}(t) = 0)$ are considered. Note also that for zero tilting $(\chi = 0$, i. e., rigid DW line), the Tilt-1DM equations reduce to the model used in Ref. 7 (hereafter referred to as Rigid-1DM), and the DW energy density is also the same as in Ref. 43. The system of three coupled Eqs. (9)–(11) form the Tilt-1DM and were numerically solved by means of a 4th order Runge-Kutta algorithm with a time step of 1 ps.

IV. RESULTS AND DISCUSSION

A. 1DM results: Temporal evolution of the DW position and DW angles

DW motion, with the same parameters as in Figs. 2 and 3, was computed by using the Tilt-1DM (9), (10), and (11), and the results for the same current $(j_a = +0.1 \times 10^{12}$ A/m$^2)$ are shown in Fig. 5. For the weak DMI Ta case, the temporal evolution of the position predicted by the 1DM and shown in Fig. 5(a), reproduces accurately the full μM results of Fig. 2(a). The temporal evolution of the DW angles, both Φ and χ, is shown in Fig. 5(b), which indicates that the DW propagates with a rigid configuration close to the Bloch state, where $\vec{m}_{DW} \approx m_{DW,x}\vec{u}_x + m_{DW,y}\vec{u}_y$ with $|m_{DW,y}| \gg |m_{DW,x}|$. However, it is the x-component of the internal DW magnetization $(m_{DW,x})$ which determines both the magnitude of the DW velocity and the direction of the CIDWM. The SHE torque on the DW is equivalent to the one of an out-of-plane effective field proportional to the x magnetization component:[7,43] $\vec{H}_{SH} \propto H_{SH}\vec{m}_{DW} \times \vec{u}_y = H_{SH}m_{DW,x}\vec{u}_z$, with H_{SH} given by Eq. (8). Note that for $m_{DW,x} < 0$ (up-down wall), $\theta_{SH} < 0$ (Ta sample), $e < 0$, and $j_a = +0.1 \times 10^{12}$ A/m^2, the factor $H_{SH}m_{DW,x}$ is negative, so the DW propagates along the electron flow, with negative velocity $(-\vec{u}_x)$. The SHE

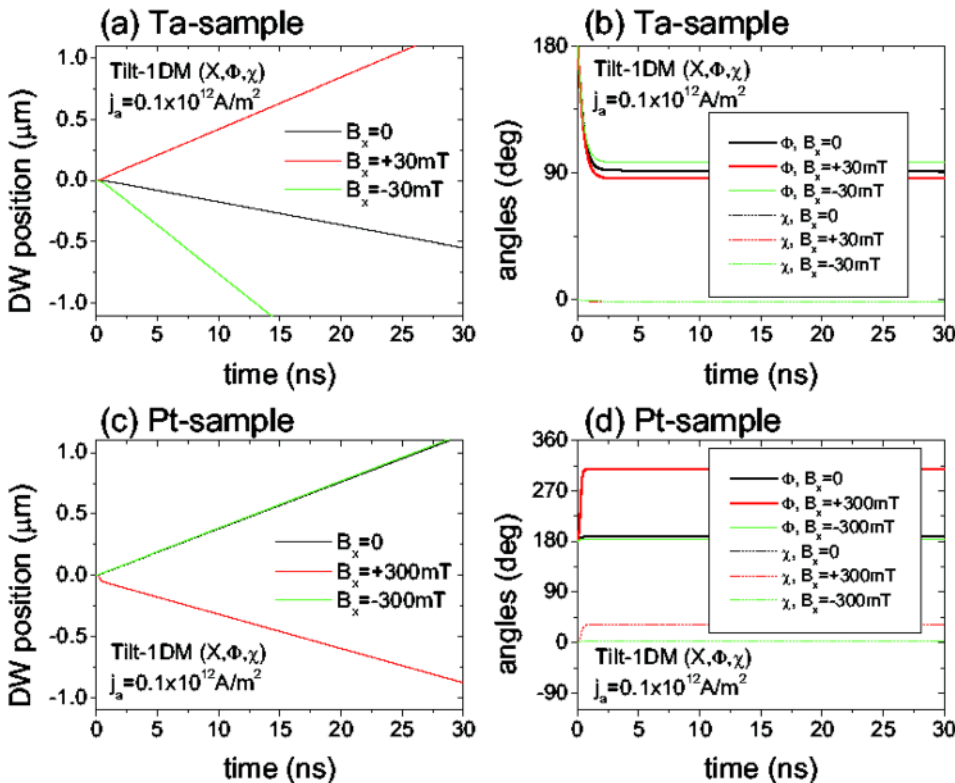FIG. 5. Tilt-1DM (X, Φ, χ) results of the current-driven DW dynamics for both the Ta $(D = -0.05$ mJ/m^2, $\theta_{SH} = -0.11$, $\alpha = 0.03)$ and Pt $(D = -1.2$ mJ/m^2, $\theta_{SH} = +0.07$, $\alpha = 0.3)$ samples. The applied current is $j_a = +0.1 \times 10^{12}$ A/m^2 and different longitudinal fields B_x are evaluated. The temporal evolution of the DW position $X(t)$ is shown in (a) and (c) for Ta and Pt samples. The temporal evolution of the DW angles Φ and χ is depicted in (b) and (c), respectively. All results correspond to an up-down configuration.

effective field drives the Neel wall, but it also exerts a torque which rotates the internal DW magnetization away from the perfect Neel state, and the rotation increases with the applied current j_a. For high enough currents (note that $j_a = 0.1 \times 10^{12}$ A/m^2 is relatively high for the weak DMI Ta sample, as will be explained later), the SHE torque is so high that the internal DW magnetization has rotated closely to the y-axis. In the absence of longitudinal field ($B_x = 0$), the terminal DW angle is $\Phi \approx 92°$ (see Fig. 5(b)), so the internal DW moment has a small but finite negative component along the x-axis ($m_{DW,x} \approx -0.035$), and therefore, the DW propagates driven by the SHE torque along the electron flow (with DW velocity along $-\vec{u}_x$). A negative longitudinal field ($B_x = -30$ mT) supports the DMI effective field $\vec{H}_D$ making the terminal DW angle larger: $\Phi \approx 98°$ (see Fig. 5(b)) so that $m_{DW,x} \approx -0.13$ and again the DW propagates along $-\vec{u}_x$ with higher velocity (see Figs. 2(a) and 5(a)). By contrast, a positive longitudinal field ($B_x > 0$) acts against the DMI field, and if strong enough ($B_x > \mu_0 |H_D|$) the direction of the DW motion reverses. For $B_x = +30$ mT, the terminal DW angle is $\Phi \approx 86°$ so that the internal DW moment along the x-axis becomes positive $m_{DW,x} \approx +0.07$, and therefore, the DW moves along the current (positive velocity along $+\vec{u}_x$). On the other hand, it is also interesting to note that regardless of B_x, no DW tilting ($\chi \approx 0$) is predicted by the Tilt-1DM (see Fig. 5(b)), in good agreement with former full μM results of Figs. 2(b)–2(d).

Figs. 5(c) and 5(d) present the Tilt-1DM results corresponding to the micromagnetic study of Fig. 3 for the Pt sample with strong DMI. Under the same current density, the DW dynamics along this strong DMI Pt sample is significantly different from the one described above for the weak DMI Ta sample. Good qualitative agreement is obtained between the μM and Tilt-1DM models, although it is only quantitatively satisfactory for zero and longitudinal fields along the positive x-axis ($B_x \geq 0$ with $B_x < 350$mT). Both for $B_x = 0$ and $B_x = -300$ mT, the internal DW magnetization points mainly along $x < 0$ corresponding to the up-down wall with left-handed chirality ($\vec{m}_{DW} \approx -\vec{u}_x$), as due to the strong negative DMI ($D < 0$), and therefore, the DW is driven along the current ($+\vec{u}_x$) because of the SHE torque on the internal DW magnetization: $\vec{H}_{SH} \propto H_{SH} \vec{m}_{DW} \times \vec{u}_y = +H_{SH} m_{DW,x} \vec{u}_z$ (take into account the positive spin Hall angle for the Pt ($\theta_{SH} = +0.07$), the negative value of the electron charge ($e < 0$) and that $m_{DW,x} < 0$ for an up-down DW under low current). Although this Tilt-1DM also takes into account the DW tilting, there are still quantitative discrepancies in the DW velocity with the full μM for both $B_x = 0$ and $B_x = -300$ mT (see Figs. 3(a) and 5(c)). Fig. 5(d) indicates negligible DW tilting ($\chi \approx 0$), but full μM results of Figs. 3(b) and 3(c) depict a significant DW tilting even for both $B_x = 0$ and $B_x = -300$ mT, respectively. On the other hand, under a strong positive longitudinal field larger than the DMI effective field ($B_x = +300$mT $> \mu_0 H_D$), the x component of the internal DW magnetization becomes positive $m_{DW,x} > 0$. This reversal of the DW chirality results in a CIDWM along the electron flow ($-\vec{u}_x$). In this case ($B_x = +300$mT), a good agreement between the Tilt-1DM and the full μM results can be clearly seen by comparing full

μM (Figs. 5(c) and 5(d)) and Tilt-1DM results (Figs. 3(a) and 3(d)). For instance, the Tilt-1DM predicts a terminal DW angle $\Phi \approx 308°$ and tilting angle $\chi \approx 32°$ (see Fig. 5(d)), which are in good qualitative agreement with full μM results (see Fig. 3(d)).

B. μM and 1DM results for the terminal DW velocity and DW angles

The former results indicate that the DW reaches a steady regime with a terminal velocity v_T. Now, we focus our attention on describing this terminal DW velocity v_T as a function of the applied current j_a in the presence of longitudinal (B_x) and transverse (B_y) fields for up-down Dzyaloshinskii walls. Our interest here is to evaluate the validity range of the 1DM description as compared to the full μM study. With this aim, the results of the Rigid-1DM (X, Φ) are also plotted along with the Tilt-1DM (X, Φ, χ) and μM results. The Rigid-1DM was already used to qualitatively describe experimental observations,[7] and it can be obtained as a particular case of the Tilt-1DM by considering zero tilting angle of the DW plane, so the DW dynamics is just given by two coupled Eqs. (9) and (10) with $\chi = 0$. The results for the Ta-sample are shown in Figs. 6(a) and 6(b) for longitudinal (B_x) and transverse (B_y) fields, respectively. In this weak DMI case, the Rigid-1DM (solid lines) predicts exactly the same results as the Tilt-1DM (small open symbols with dashed lines), and it is also in excellent quantitative agreement with full μM results (large filled symbols). These results confirm the negligible role of the DW tilting for weak DMI samples, as it was also addressed by our experimental and static analysis in Ref. 43.

On the other hand, Figs. 6(a) and 6(b) clearly show the two regimes for the terminal DW velocity: a low-current regime ($|j_a| < 0.03 \times 10^{12}$ A/m^2), where the DW velocity increases linearly with j_a, and a high-current regime ($|j_a| > 0.2 \times 10^{12}$ A/m^2) where the DW velocity saturates as j_a increases. The low-current regime is related to the spin Hall effective field which drives the initial Neel walls ($\vec{m}_{DW} = -\vec{u}_x$) along the electron flow due to the negative $\theta_{SH} = -0.11$ of Ta. In the low current regime, the internal DW moment has both x and y components but the latter is small: $\vec{m}_{DW} = m_{DW,x} \vec{u}_x + m_{DW,y} \vec{u}_y$ with $m_{DW,x} < 0$ and $|m_{DW,x}| \gg |m_{DW,y}|$. As the current increases, the internal DW magnetization deviates from the perfect Neel state so the magnitude of the x component ($|m_{DW,x}|$) decreases and the y component ($|m_{DW,y}|$) increases. Under sufficiently high currents and in the absence of in-plane fields ($B_x = B_y = 0$), the DW adopts a terminal quasi-Bloch configuration with $|m_{DW,y}| \gg |m_{DW,x}|$, and the terminal velocity saturates as j_a increases (see Fig. 6(a)) because the driving SHE effective field $\vec{H}_{SH}$ scales with the product $j_a |m_{DW,x}|$: $|m_{DW,x}| \rightarrow 0$ as $j_a \rightarrow \infty$ keeping the product constant. In the presence of in-plane fields (see Figs. 6(a) and 6(b)), the terminal DW velocity also saturates in the high current regime, but the longitudinal field B_x can reverse the direction of the CIDWM as already discussed in Sec. IV A. Note that, as also explained in Sec. IV A, the magnitude of the terminal DW velocity is larger (smaller) when B_x points in the same (opposite)
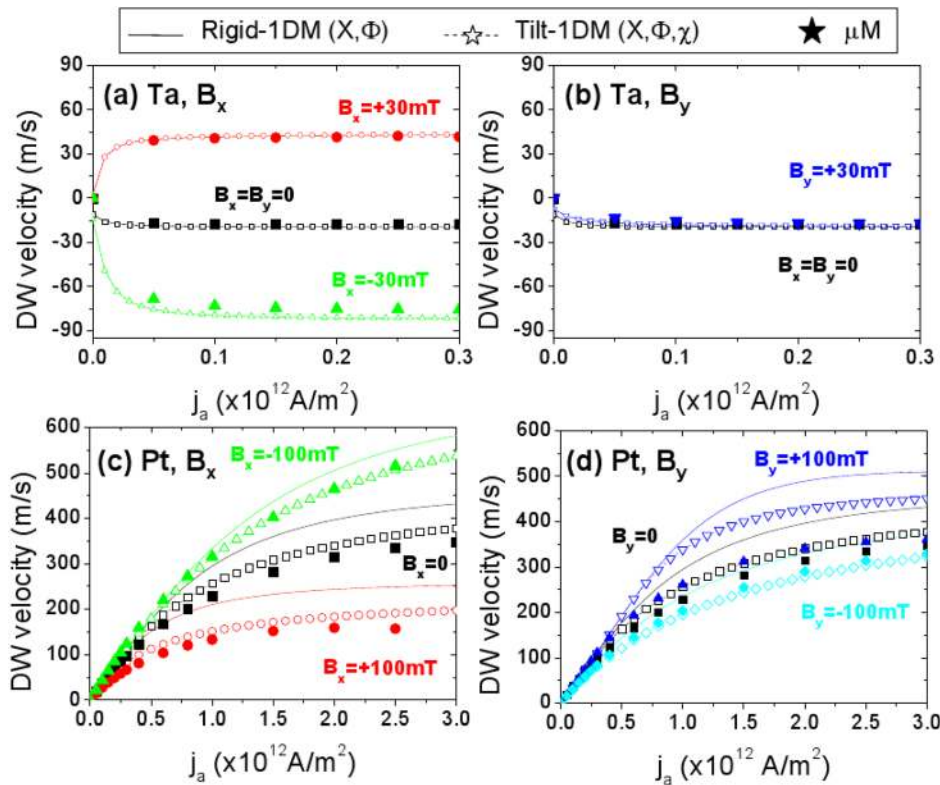
FIG. 6. DW velocity as a function of j_a in presence of in-plane fields for both the Ta ((a) and (b)) and Pt ((c) and (d)) samples. (a) and (c) correspond to longitudinal fields (B_x) and (b) and (d) correspond to transverse fields (B_y). The Rigid-1DM (X, Φ) (solid lines), the Tilt-1DM (X, Φ, χ) (lines with small open symbols) and full micromagnetic (μM, large filled symbols) results are compared for each case. All results correspond to an up-down configuration.

direction as the $\mu_0 \vec{H}_D$. As shown in Fig. 6(b), the finite and constant terminal velocity observed under high currents in the presence of transverse fields ($B_y \neq 0$) is the same as in the absence of the transverse fields ($B_y = 0$) which further support our description and interpretation.

The terminal DW velocity v_T as a function of j_a for up-down Dzyaloshinskii walls along the strong DMI Pt sample was also evaluated in the presence of in-plane fields. The results computed from the Rigid-1DM (solid lines), the Tilt-1DM (small open symbols with dashed lines), and the full μM (large filled symbols) are shown in Figs. 6(c) and 6(d) for both B_x and B_y in-plane fields with fixed amplitude of $|B_x| = |B_y| = 100 \text{mT}$ and different polarities. In the low-current linear regime ($|j_a| < 0.2 \times 10^{12} \text{A/m}^2$), the three sets of results are indistinguishable. As expected, the discrepancies between the Rigid-1DM and the μM results increase with increasing j_a, because also the DW tilting increases. A similar analysis was also carried by Boulle *et al.*[42] for other material parameters but only for transverse fields with a fixed polarity. Similar to Ref. 42, our results also indicate that in general, the Rigid-1DM tends to overestimate the current-driven DW velocity predicted by full μM simulations (see for instance, Fig. 6(c) for $B_x = +100 \text{mT}$ under high currents), and from Figs. 6(c) and 6(d) it seems that the Tilt-1DM provides a better approach to these full 3D micromagnetic results for high-DMI samples. However, as will be discussed later, we also find noticeable qualitative differences between the Tilt-1DM and the full μM results.

Before addressing these issues, the terminal DW velocity along the Ta sample as a function of B_x and B_y is shown in Figs. 7(a) and 7(b), respectively, under a fixed current ($j_a = 0.1 \times 10^{12} \text{A/m}^2$). Again for this weak DMI sample, the Rigid-1DM (solid lines) predicts exactly the same results as

the Tilt-1DM (small open symbols with dashed lines), and both are also in excellent quantitative agreement with full μM results (large filled symbols), confirming again the negligible role of the DW tilting for weak DMI samples and the quantitative validity of the Rigid-1DM.

In the presence of SHE and low-DMI ($D \neq 0$ but $|D|$ small, so that $\chi \approx 0$) and for $P = 0$, the most general 1DM solution in the steady-state regime ($\dot{\Phi} = 0$) for $H_z = 0$ takes the form

$$\dot{X} = \frac{\gamma_0 \Delta}{\alpha} \frac{\pi}{2} Q H_{SH} \cos\Phi \qquad (15)$$

and

$$\tan\Phi = \frac{\pi}{2\alpha} \frac{Q H_{SH} + \alpha H_y}{\frac{\pi}{2}(Q H_D + H_x) - H_K \cos\Phi}. \qquad (16)$$

In the case $|H_D + H_x| \gg H_K$, approximate analytical expressions can be obtained for the terminal DW velocity $v_T \equiv \dot{X}(t \to \infty)$. In the absence of in-plane fields ($H_x = H_y = 0$), the terminal velocity is[33]

$$v_T = \gamma_0 \Delta \frac{\pi}{2} \frac{H_D}{\sqrt{1 + \left(\frac{\alpha H_D}{H_{SH}}\right)^2}}. \qquad (17)$$

From (17) two different regimes are deduced depending on the relative amplitude of H_{SH} versus αH_D. For low currents ($H_{SH} \ll \alpha H_D$, or $j_a \ll j_{th} \equiv \frac{2eL_z \alpha D}{\hbar \theta_{SH} \Delta}$), the DW velocity is limited by the SHE[43]

$$v_{T,SHE} \approx \frac{\gamma_0 \Delta}{\alpha} \frac{\pi}{2} H_{SH}, \qquad (18)$$
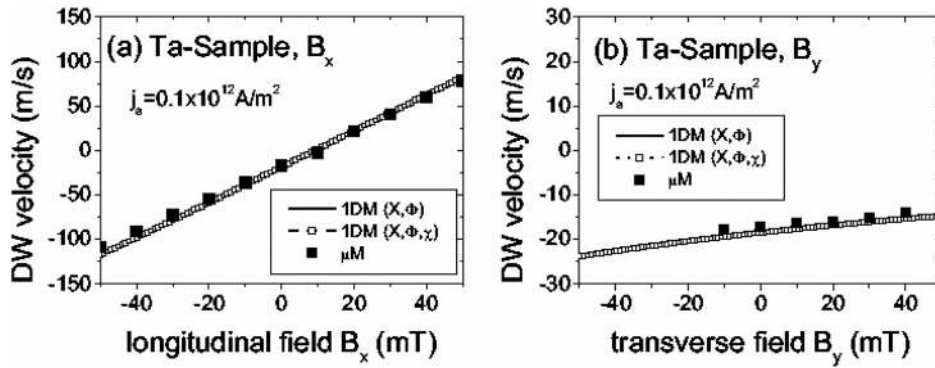
FIG. 7. DW velocity along the Ta-sample ($D = -0.05$ mJ/m^2, $\theta_{SH} = -0.11$, $\alpha = 0.03$) as function of the in-plane fields for a fixed current of $j_a = 0.1 \times 10^{12}$ A/m^2: (a) longitudinal fields (B_x) and (b) transverse fields (B_y). The Rigid-1DM (X, Φ) (solid lines), the Tilt-1DM (X, Φ, χ) (lines with small open symbols), and full micromagnetic (μM, large filled symbols) results are compared for each case. All results correspond to an up-down configuration.

whereas for high currents $j_a \gg j_{th}$, the DW velocity is DMI-limited as it saturates towards[43]

$$v_{T,DMI} \approx \gamma_0 \Delta \frac{\pi}{2} H_D. \qquad (19)$$

Considering the parameters of the Ta-sample, the transition between these two regimes occurs at $j_{th} \approx 3 \times 10^9$ A/m^2, in good agreement with all former 1DM and μM results. Therefore, a current $j_a = 0.1 \times 10^{12}$ A/m^2 is well above than that threshold and the terminal DW velocity predicted by (19) is -19.73 m/s, which is close to the value obtained from full μM simulations (-18.73 m/s, see Fig. 7).

In the presence of longitudinal fields H_x, Eq. (17) is modified to[43]

$$v_T = \gamma_0 \Delta \frac{\pi}{2} \frac{H_D + H_x}{\sqrt{1 + \left(\frac{\alpha(H_D + H_x)}{H_{SH}}\right)^2}} \qquad (20)$$

and for the DMI-limited regime, the terminal DW velocity (19) becomes[43]

$$v_{T,DMI} \approx \gamma_0 \Delta \frac{\pi}{2} (H_D + H_x), \qquad (21)$$

which predicts quite accurately the strong linear dependence depicted in Fig. 7(a).

Under transverse fields H_y, the terminal DW velocity is most conveniently written as[43]

$$v_T = -\frac{\gamma_0 \Delta}{\alpha} \frac{\pi}{2} \frac{H_{SH}}{\sqrt{1 + \left(\frac{H_{SH} + \alpha H_y}{\alpha H_D}\right)^2}}. \qquad (22)$$

It is straightforward to confirm that this approximate expression (22) also reproduces quite accurately the 1DM and the full μM results depicted in Fig. 7(b).[70] It is interesting to note that (22) indicates that v_T exhibits a peak at $H_y = -H_{SH}/\alpha$ and tends to zero for larger $|H_y|$. For the Ta-sample, the peak occurs at $B_y = \mu_0 H_y = -287.7$ mT, which is far from the range studied in Fig. 7(b), and where the velocity reaches $v_T = -604$ m/s (not shown).

Let us focus now on the strong DMI Pt sample. A similar analysis to the one shown in Fig. 7 for the weak DMI Ta-sample was also carried out for the Pt-sample considering the same current ($j_a = 0.1 \times 10^{12}$ A/m^2). The field

dependence of the terminal DW velocity is depicted in Figs. 8(a) and 8(b) for B_x and B_y, respectively. The DW angles as a function of both B_x and B_y (only Φ for the Rigid-1DM, and both Φ and χ for both the Tilt-1DM and μM) are also compared in Figs. 8(c) and 8(d), where the micromagnetic DW angle Φ was computed by averaging over the strip width L_y.

In contrast to the 1D models, which are mathematically valid for any magnitude of j_a, B_x, and B_y, the micromagnetic modeling shows that thresholds exist beyond which the domains and DW structure are no longer stable: (i) Under large $|B_x|$ and $|j_a|$, the SHE torque destabilizes the domains. With $j_a = 0.1 \times 10^{12}$ A/m^2, longitudinal fields $|B_x| > 350$mT cause the DW to vanish and the domain magnetization to orient nearly parallel to the applied field within the first ~ 1 ns of simulation time. (ii) For transverse fields $|B_y| > 150$mT, the DW tilting angle reaches $\chi \approx 90°$ and therefore, the DW extends along the strip axis (x), so DW motion along the x-axis no longer occurs. Therefore, the full μM results described hereafter will be restricted to limited ranges: -300mT $\leq B_x \leq +300$mT and -125mT $\leq B_y \leq +125$mT in order to preserve the DW and its dynamics. Note that these restrictions on the in-plane fields do not apply for the 1D models.

Aside from the large positive transverse fields $B_y \geq 100$mT, the Tilt-1DM provides a closer agreement with the μM terminal DW velocity than the Rigid-1DM does, although both 1D models describe qualitatively similar results (see Fig. 8(b)) in the micromagnetic limited range (-125mT $\leq B_y \leq +125$mT). Under transverse fields (Fig. 8(d)), both the Rigid and the Tilt 1D models are also in qualitative agreement with μM for the DW angle Φ. As expected, the Tilt-1DM provides a more accurate description of the μM than the Rigid-1DM, but significant quantitative differences are still evident; whereas the μM computed Φ abruptly reaches 90° for $|B_y| > 125$mT, both 1D models predict a much more smooth DW moment rotation, requiring transverse fields in the order of $|B_y| = 400$mT to rotate the internal DW magnetization angle to 90°. It is also clear from Fig. 8(d) that the Tilt-1DM significantly underestimates the tilt angle χ as compared to the full μM simulations. The μM computed steady states under representative transverse fields are shown in Figs. 9(f)–9(i). These μM snapshots clearly indicate the calculations based on the Tilt-1DM only describes the μM results in a qualitative fashion for strong DMI-samples. For instance, the Tilt-1DM assumes that all magnetic moments within the DW rotate uniformly, whereas
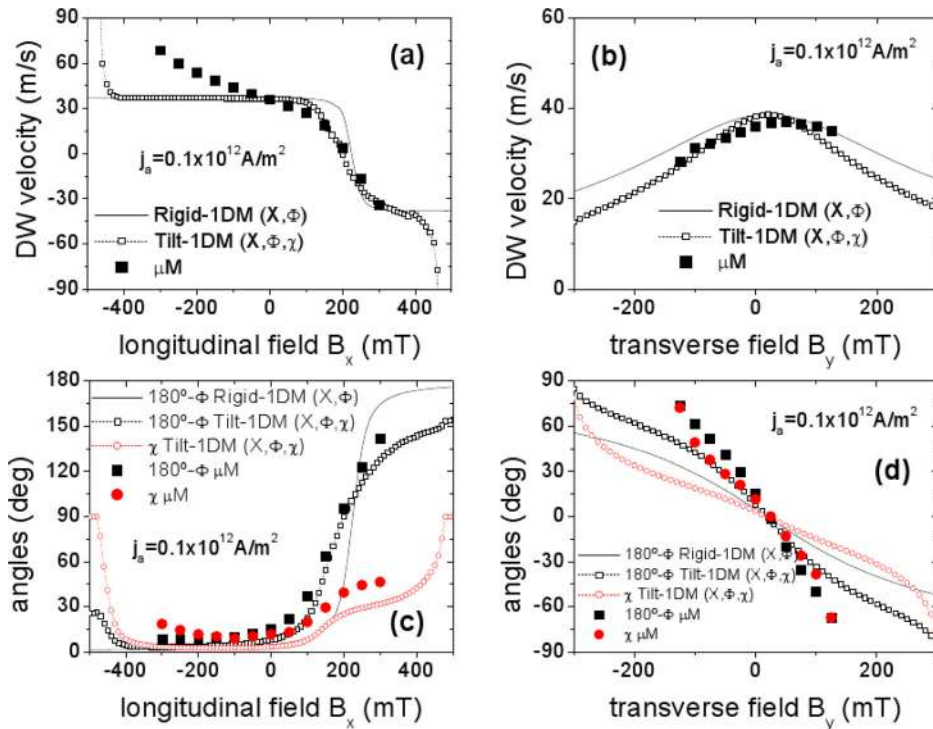
FIG. 8. DW velocity along the Pt-sample ($D = -1.2$ mJ/m^2, $\theta_{SH} = +0.07$, $\alpha = 0.3$) as function of the in-plane fields for a fixed current of $j_a = 0.1 \times 10^{12}$ A/m^2: (a) longitudinal fields (B_x) and (b) transverse fields (B_y). The DW angles dependence on B_x and B_y is shown in (c) and (d), respectively. All results correspond to an up-down configuration. The Rigid-1DM (X, Φ) (solid lines), the Tilt-1DM (X, Φ, χ) (lines with small open symbols), and full micromagnetic (μM, large filled symbols) results are compared for each case.

μM results indicate that these moments exhibit some distribution of the rotation angles (see Figs. 9(f)–9(i)). Moreover, a DW in the Tilt-1DM acts as a rigid line when it tilts, whereas the micromagnetically computed DW profile is not a rigid line and exhibits bowing in the tilting process (see Figs. 9(f)–9(i)). In short, the non-uniform DW angle and the non-uniform DW tilting across the strip width cannot be described by the Tilt-1DM.

Regarding longitudinal fields (B_x), the Tilt-1DM provides a more accurate prediction of the μM results than the Rigid-1DM does for positive fields below +300 mT (see Fig. 8(a)), so the inclusion of the DW tilting provides a smoother transition from positive to negative terminal velocity, related to the longitudinal field-induced reversal of the DW chirality. Also, the field dependence of the DW angles Φ and χ is

qualitatively described by the Tilt-1DM for positive fields smaller than +300 mT (see Fig. 8(c)), although quantitative discrepancies are again evident even for the low current density evaluated here ($j_a = 0.1 \times 10^{12}$ A/m^2). For negative longitudinal fields ($B_x < 0$), however, both the Tilt and the Rigid 1D models predict the same plateau of the terminal DW velocity in the micromagnetic limited range (-300mT $\leq B_x \leq 0$), whereas the full μM results indicate a monotonic increase of DW velocity from $B_x = 0$ to $B_x = -300$ mT. These μM results are in good qualitative agreement with several experimental measurements.[7,8,43] The Tilt-1DM also predicts an increase of the terminal DW velocity for very large negative fields ($B_x < -400$mT). However, as stated above, the magnitude of these fields is larger than the threshold above which the micromagnetic simulations indicate that the domain structure is destabilized by the spin Hall torque, so that the domain wall vanishes and the magnetization aligns closely with the longitudinal field.

Another discrepancy is also observed for the tilt angle χ under negative longitudinal fields (see Fig. 8(c)): the tilt-1DM predicts a monotonic decrease of χ from $B_x = 0$ to $B_x = -300$ mT, whereas the micromagnetic model indicates that χ reaches a minimum for $B_x \approx -100$mT, and that the tilt angle χ increases again for smaller fields, from $B_x = -100$ mT to $B_x = -300$ mT. The partial alignment of magnetization along B_x in the two domains at both sides of the DW is evident in the m_x snapshots depicted Figs. 3(c) and 3(d) for both $B_x = -300$ mT and $B_x = +300$ mT, respectively, as compared to the zero field case (Fig. 3(b)). μM simulations for larger longitudinal fields $|B_x| > 300$mT indicate sample magnetization becomes aligned along x-axis. All these differences between the Tilt-1DM and the μM results suggest that a full μM analysis of the experimental studied samples is required to gain a better quantitative description of the current-induced DW motion along strong-DMI
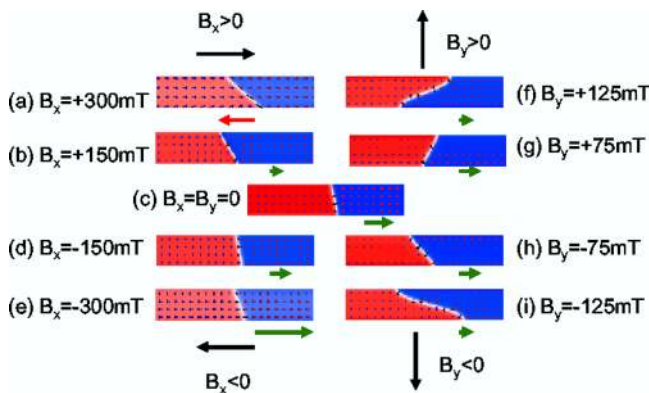

FIG. 9. Micromagnetic snapshots of the steady-state up-down DW configurations along the Pt-sample driven by a fixed current of $j_a = 0.1 \times 10^{12}$ A/m^2 and several in-plane fields: left and right columns correspond to longitudinal B_x and transverse B_y fields, respectively. The arrows below each snapshot indicate the direction of the DW motion: toward to right green arrows mean DW motion along current whereas toward to the left red arrows mean DW motion along the electron flow.

samples such as the Pt-sample evaluated here. Indeed, the boundary conditions imposed by the DMI at the sample surface, the in-plane component of the magnetization in the domains under the strong in-plane field applied for strong-DMI samples, and the non-uniform distribution of the DW angles (Φ and χ) may play a significant role on quantifying the DW velocity in high-DMI samples. As outlined above in the previous paragraph for in-plane fields, none of these aspects can be explained by the Tilt-1DM.

It is possible, however, to explain the main cause of discrepancy between the Tilt-1DM and μM in strong-DMI samples in the presence of longitudinal fields pointing along the inherent DW moment, that is, under negative fields $B_x < 0$ for the left-handed up-down walls (see. Fig. 8(a)). For this purpose, we can obtain the steady-state ($\dot{\Phi} = \dot{\chi} = 0$) DW velocity from the Tilt-1DM Eqs. (9)–(11). For $P = 0$ and $H_z = 0$, the general solution for the DW velocity in the steady-state regime ($\dot{\Phi} = \dot{\chi} = 0$) takes the form

$$\dot{X} = \frac{\gamma_0 \Delta}{\alpha \cos \chi} \frac{\pi}{2} Q H_{SH} \cos \Phi, \tag{23}$$

which is analogous to the expression (15) obtained from the Rigid-1DM, but now including the DW tilting, which scales the terminal velocity by a factor of $1/\cos\chi$. In the framework of the Tilt-1DM, the terminal DW angles Φ and χ are the solutions of (10) and (11) by imposing $\dot{\Phi} = \dot{\chi} = 0$. These solutions are much more complicated than the corresponding general solution for the terminal Φ in the Rigid-1DM given by Eq. (16), but numerical solutions to the equations would yield the results already depicted in Fig. 8(c) by open symbols. In general, the Tilt-1DM underestimates the micromagnetically computed angles $\Phi_{\mu M}$ and $\chi_{\mu M}$ (filled symbols in 8(c)), so we have considered these more realistic values as inputs for the analytical expression of the terminal DW velocity (23), first maintaining the analytical value of the DW width deduced from $\Delta = \sqrt{A/K_{eff}} \approx 7.62$nm. The terminal velocity results computed from (23) with ($\Phi_{\mu M}$, $\chi_{\mu M}$, $\Delta = 7.62$nm) for the negative field range (-300mT $\leq B_x \leq 0$) under the same fixed current density ($j_a = 0.1 \times 10^{12}$ A/m^2) are depicted in Fig. 10(a) by red circles, which indicate that the DW velocity still remains constant similarly to the predictions by both the Tilt and the Rigid 1D models already shown in Fig. 8(a).

This fixed-DW width analysis points out that the underestimation of the steady-state DW angles cannot be the main cause of the strong monotonic increase of the terminal DW velocity for -300mT $\leq B_x \leq 0$ as deduced from full μM (black squares in Figs. 8(a) and 10(a)). However, according to (23), the terminal DW velocity in the low-current (SHE-limited) regime is also proportional to the DW width Δ. In order to evaluate its influence on the terminal DW velocity, the DW width was micromagnetically computed ($\Delta_{\mu M}$) according to the Thiele definition for the steady-states corresponding to $j_a = 0.1 \times 10^{12}$ A/m^2 and -300mT $\leq B_x \leq 0$. The results are in Fig. 10(b), and they indicate a monotonic increase of DW velocity as B_x decreases. When these micromagnetic values of the steady-state DW width ($\Delta_{\mu M}$) are considered as an additional input, the terminal DW velocity
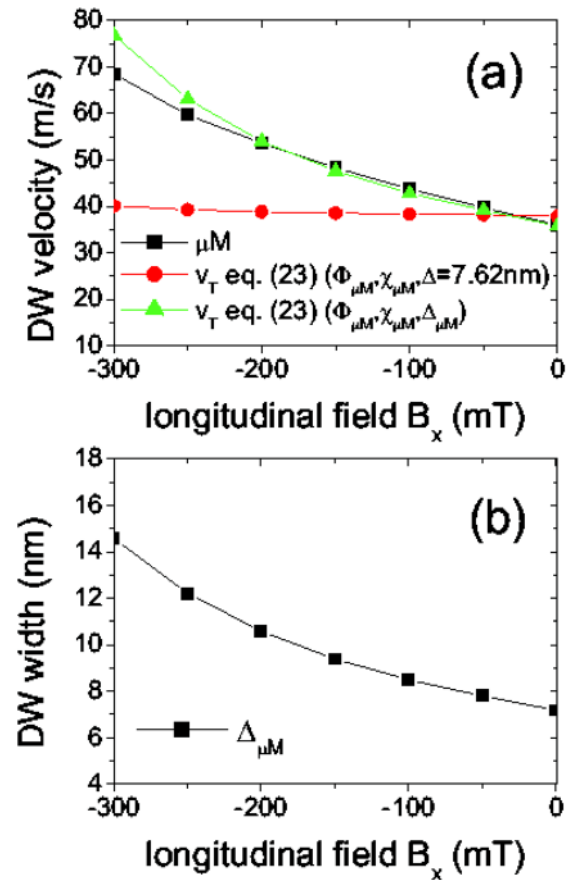

FIG. 10. Analysis of discrepancy between the Tilt-1DM and full μM terminal DW velocity results for the low-current ($j_a = 0.1 \times 10^{12}$ A/m^2) induced DW motion in the presence of negative longitudinal fields $B_x < 0$, parallel to the inherent DW moment for a strong-DMI up-down wall with left-hand chirality. (a) Terminal DW velocity as function of $B_x < 0$: Black squares correspond to full μM. Red circles are the results obtained from Eq. (23) by using the micromagnetically computed values of the steady-state DW angles ($\Phi_{\mu M}$, $\chi_{\mu M}$) of Fig. 8(c) with fixed DW width $\Delta = 7.6$ nm. Green triangles are the results obtained from Eq. (23) by using the micromagnetically computed values of the steady-state DW angles ($\Phi_{\mu M}$, $\chi_{\mu M}$) of Fig. 8(c) and the DW width represented in Fig. (b). (b) Micromagnetically computed DW width ($\Delta_{\mu M}$) in the steady-state regime.

predicted by Eq. (23) and shown by green triangles in Fig. 10(a) matches remarkably the full μM results (black symbols in Fig. 10(a)). This analysis points out that when in-plane longitudinal fields are applied in the same direction as the inherent DW moment imposed by the strong DMI, the DW width increases resulting in a strong increase of the terminal DW velocity as $|B_x|$ increases. Note that these μM results are in good qualitative agreement with several experimental measurements,[7,8,43] where the DW velocity depicts a linear dependence on the longitudinal field.

C. Quantifying the magnitude of DMI

The analysis of the current-driven DW motion in the presence of in-plane longitudinal fields B_x is also relevant to quantifying the magnitude of the DMI, because the longitudinal field at which the direction of DW motion reverses (or at which the DW velocity becomes null) B^* is related in the 1DM to the DMI parameter D as $B^* = D/(M_s \Delta)$, where Δ is

the DW width. For the weak-DMI Ta-sample under $j_a = 0.1 \times 10^{12}$ A/m^2, the DW velocity becomes null at $B_x = B^* = 9.44$ mT (see Fig. 7(a)), and the three models predict the same value. Taking into account the DW width at rest $\Delta = 7.62$ nm and $M_s = 7 \times 10^5$ A/m, a value of $|D| = 0.05$ mJ/m^2 is estimated, which is exactly the value considered as input parameter for the weak-DMI Ta-sample study ($D = -0.05$ mJ/m^2). For the strong-DMI Pt-sample in the low current regime ($j_a = 0.1 \times 10^{12}$ A/m^2), the zero-velocity longitudinal field B^* is different between the Rigid and the Tilt 1D models: $B^*_{Rigid} \approx 225$ mT in the Rigid-1DM and $B^*_{Tilt} \approx 200$ mT in the Tilt-1DM. According to $B^* = D/(M_s\Delta)$, the Rigid-1DM predicts $|D| \approx 1.2$ mJ/m^2 (which is the same input parameter for the strong-DMI Pt-sample study), whereas the Tilt-1DM results in $|D| = 1.067$ mJ/m^2, which is 11% smaller than the input parameter. The micromagnetically computed values are in between these 1DM predictions: $B^*_{\mu M} \approx 210$ mT and $|D| = 1.12$ mJ/m^2. Therefore, the expression $B^* = D/(M_s\Delta)$ slightly underestimates the magnitude of the DMI (D). As the full micromagnetic model takes into account the 3D spacial dependence of the magnetization, it can be considered as the more realistic of the three models, and therefore, we can state that the Rigid-1DM overestimates the $B_{x,D}$ whereas the Tilt-1DM underestimates it with respect to full micromagnetic simulations, which provides the most accurate estimation for B^*.

The velocity dependence on the longitudinal field was also evaluated in the high-current DMI-limited regime for the strong DMI sample. The results for a fixed density current of $j_a = 2.5 \times 10^{12}$ A/m^2 are shown in Fig. 11(a). Although in this high current regime some quantitative differences are evidenced, both the Rigid (solid lines) and Tilt (lines with small open symbols) 1D models display trends that are qualitatively similar to those of the full micromagnetic calculations, with a strong velocity dependence on B_x for both positive and negative values. The zero-velocity longitudinal field B^* predicted by these 1D models is the same as is predicted in the low-current regime: $B^*_{Rigid} \approx 225$ mT and $B^*_{Tilt} \approx 200$ mT.

However, for the high current evaluated here ($j_a = 2.5 \times 10^{12}$ A/m^2), the range of longitudinal fields is limited to $|B_x| \leq 100$ mT in the micromagnetic framework (μM). As described previously, in the presence of large longitudinal fields (here corresponding to $|B_x| \geq 100$ mT), j_a destabilizes the domains and DW system. This is not surprising, because at sufficiently large B_x and j_a the spin Hall torque in the domains is large enough to nucleate multiple reversed domains,[71] such that a single-DW configuration is no longer stable. The instability of the DW system occurs at smaller longitudinal fields when the current is further increased. This limits the range for the micromagnetically computed DW velocity in Fig. 6(c), which prevents a determination of B^* that can be compared to the Rigid and Tilt 1DM predictions. Although DW motion and velocity reversal under large $|B_x|$ approaching 300 mT has been observed experimentally,[8] for j_a up to 2.5×10^{12} A/m^2, we are unable to reproduce such behavior micromagnetically using the present material parameters due to destabilization of the domain structure within ~1 ns of current pulse application.
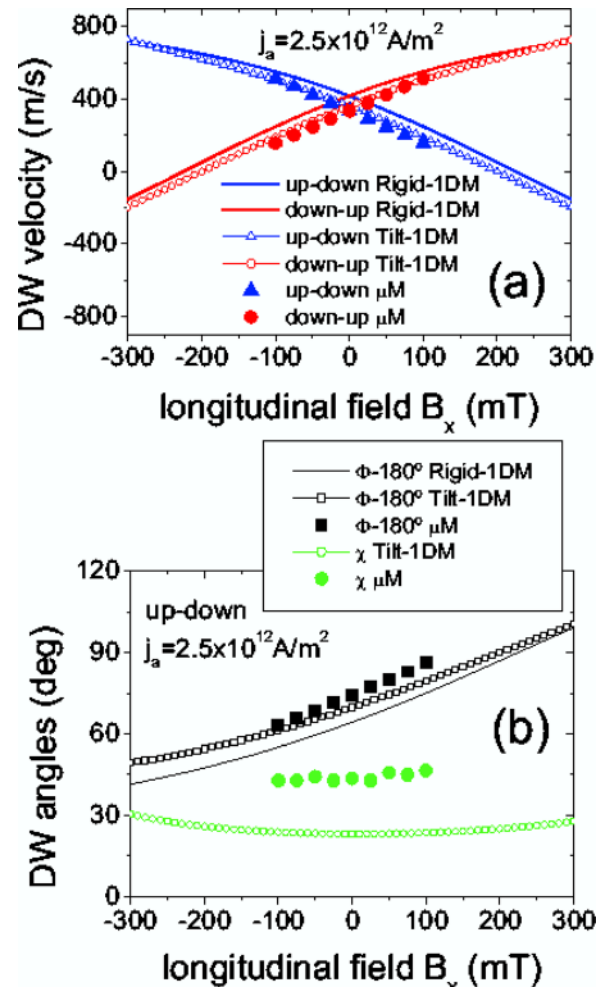

FIG. 11. (a) DW velocity along the Pt-sample ($D = -1.2$ mJ/m^2, $\theta_{SH} = +0.07$, $\alpha = 0.3$) as function of the longitudinal field B_x for a high current of $j_a = 2.5 \times 10^{12}$ A/m^2. (b) DW angles dependence on B_x. The Rigid-1DM (X, Φ) (solid lines), the Tilt-1DM (X, Φ, χ) (lines with small open symbols), and full micromagnetic (μM, large filled symbols) results are compared for each case.

Within the micromagnetically accessible range of B_x ($|B_x| < 100$ mT for $j_a = 2.5 \times 10^{12}$ A/m^2), although the micromagnetically computed velocities track reasonably closely to the Tilt and Rigid 1DM calculations (Fig. 11(a)), it is seen in Fig. 11(b) that the micromagnetically computed tilt angles are significantly larger than those predicted by the Tilt-1DM. With $B_x = 0$, the micromagnetic results yield $\chi_{\mu M} \approx 45°$, whereas the tilt-1DM yields $\chi_{Tilt-1DM} \approx 22°$. These results highlight the need for a full micromagnetic treatment for quantitative analysis of experimental results.

D. μM simulations of realistic samples: Edge roughness and thermal effects

The preceding results were carried out by considering ideal defect-free samples at zero temperature. However, in out-of-plane magnetized thin films, DWs driven by weak driving fields or currents can interact strongly with defects, and the line profiles of such DWs moving by thermal activation can be irregular. For example, a rough DW line may have multiple angles along its length or DW tilting may result due to pinning. Here, we show through micromagnetic

simulations that DW tilting occurs due to strong DMI even in the presence of thermally activated motion through disorder and that the tilting behavior is not qualitatively altered under realistic pinning conditions.

Full micromagnetic simulations were performed by considering disorder and thermal effects at $T = 300$ K. Thermal fluctuations are micromagnetically simulated by adding a random stochastic field $\vec{H}_{th}$ to the deterministic effective $\vec{H}_{eff}$ in Eq. (1). $\vec{H}_{th}$ is an uncorrelated Gaussian-distributed random vector with zero mean value (see Ref. 68 for further details on its statistical properties and magnitude H_{th}). The same cell size and time step as in the free-defect and zero temperature case were considered. The disorder was taken into account by assuming an edge roughness with a typical grain size of $D_g = 4$ nm on both sides of the strip (see Ref. 68 for further details). Such random disorder is qualitatively consistent with nano-scale defects distributed throughout experimentally measured strips.[43] The dimensions here are the same as those for the case without pinning and thermal activation, and the same material parameters as the strong DMI Pt-sample are used. Here, we restrict the analysis to the representative results for the strong-DMI Pt sample.[72]

Due to the random edge roughness, the DW experiences pinning against its free propagation. A minimum out-of-plane field of $B_{z,min} = B_d = 11.2$ mT, or minimum current density of $j_{a,min} = j_d = 0.14 \times 10^{12}$ A/m^2, is required to propagate the DW at $T = 0$. By contrast, at $T = 300$ K, the DW propagates by thermal activation even under B_z or j_a lower than these threshold values. Here, we focus our attention to the current-driven case, and in order to qualitatively describe the experimentally observed thermally activated DW dynamics,[43] we have simulated DW motion driven by a sub-threshold current density ($j_a = 0.10 \times 10^{12}$ A/m^2) in the rough strip ($D_g = 4$ nm) at $T = 300$ K. Typical temporal evolution of the DW position of the thermally activated DW motion for this fixed sub-threshold current density ($j_a = 0.10 \times 10^{12}$ A/m$^2 < j_d$, which is around 28% smaller than the deterministic depinning threshold) are

shown in Figs. 12(f) and 12(g) in the presence of longitudinal and transverse field, respectively. In this case, the DW propagates along the strip in an irregular fashion: it propagates until it reaches a position with strong pinning and remains there for some time until the thermal activation eventually assists the local DW depinning, and the DW starts propagating again. Since the applied current density ($j_a = 0.10 \times 10^{12}$ A/m^2) is smaller but close to the deterministic threshold ($j_d = 0.14 \times 10^{12}$ A/m^2), thermal activation at $T = 300$ K makes the duration of each DW pinning event very short (<1 ns).

Similar to the SHE-driven DW dynamics in a defect-free strip, DW tilting is evidenced in thermally activated motion driven by a small current ($j_a < j_d$) in a rough strip. The snapshots in Fig. 12(a) depict a typical DW configuration when the DW is driven in the $+x$ direction by the SHE under a current of $j_a = +0.10 \times 10^{12}$ A/m^2. Large in-plane longitudinal B_x (Figs. 12(b)–12(f)) and transverse B_y (Figs. 11(d)–12(g)) fields —of magnitude 100 mT—modify the internal configuration during the thermally activated dynamics of SHE-driven DWs. A longitudinal field $B_x < 0$ supports the inherent internal DW magnetization in the $-x$ direction (left-handed chirality), whereas $B_x > 0$ acts against the inherent configuration. The DW propagates faster under $B_x < 0$ (green curve in Fig. 12(f)) than in the $B_x = 0$ case, whereas the DW velocity is reduced with $B_x > 0$ (red curve in Fig. 12(f)). As it was shown before for perfect samples at zero temperature, $B_x = +100$ mT is not sufficient to overcome the strong DMI and reverse the DW chirality completely, so the DW still propagates in the $+x$ direction. Both $B_x > 0$ and $B_x < 0$ contribute to the DW tilting as shown in Figs. 12(b) and 12(c). Note that the DWs under $B_x > 0$ and $B_x < 0$ both exhibit the same the rotation sense of DW tilting than in the defect-free and zero temperature case.

When a transverse field $|B_y| = 100$ mT is applied, the tilting of the DW line is even more pronounced (Figs. 12(d) and 12(e)). The internal DW magnetization prefers to align with the large transverse field, while the DMI stabilizes the magnetization perpendicular to the DW line (i.e., Neel DW),
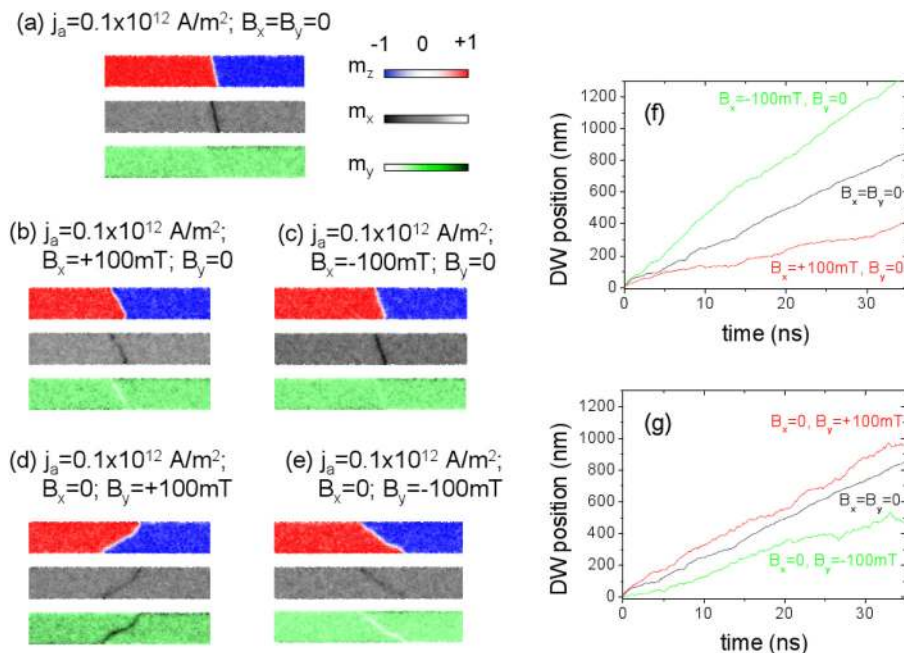

FIG. 12. Micromagnetic simulations of a realistic strip with edge roughness and at room temperature. (a)–(e) Micromagnetic snapshots of the DW configuration under strong DMI ($D = -1.2$ mJ/m^2) driven by $j_a = 0.10 \times 10^{12}$ A/m^2 in the rough strip with disorder ($D_g = 4$ nm) at $T = 300$ K and different in-plane magnetic fields. (f) and (g) Micromagnetically computed temporal evolution of the DW position under (f) in-plane longitudinal fields B_x and (g) in-plane transverse fields B_y.

resulting in the tilting of the entire DW line to accommodate both the large Zeeman and DMI energies. Therefore, $B_y > 0$ (Fig. 10(d)) and $B_y < 0$ (Fig. 10(e)) result in opposite rotations of the internal DW magnetization (i.e., $m_{DW,y}$) and the DW-line tilting.

All these micromagnetic simulations under realistic conditions (with pinning and at room temperature) indicate that the DW tilting is a dynamical effect that occurs quite generally in the presence of strong DMI. On the other hand, the DW tilting does not appear if weak DMI is considered,[72] as it is the case of the Ta/CoFe. Moreover, these simulations clearly show that roughness does not change qualitatively the tilting behavior or the mean tilt angle. On the other hand, the averaged DW velocities in the thermally activated regime are significantly reduced as compared to the ideal free-defect and zero temperature case, and this has to be taken into account to properly interpret experimental measurements carried out in this thermally activated regime. For instance, in the absence of in-plane fields $(B_x = B_y = 0)$ the averaged DW velocity under $j_a = 0.1 \times 10^{12}$ A/m^2 along a rough sample ($D_g = 4$ nm) and at room temperature ($T = 300$ K) is ≈ 24.5 m/s, which is around 32% smaller than the terminal DW velocity in the perfect zero temperature case. These differences between the realistic (random pinning and thermal fluctuations) and the ideal (perfect samples at zero temperature) conditions are also significantly pronounced in the presence of in-plane fields. In the presence of a longitudinal field of $B_x = +100$ mT, the ideal ($D_g = T = 0$) terminal velocity is ≈ 43.7 m/s, decreasing to 12.3 m/s under realistic conditions ($D_g = 4$ nm and $T = 300$ K).

V. CONCLUSIONS

The current-induced motion of Dzyaloshinskii walls with left-handed chirality has been studied by means of full micromagnetic simulations. The analysis was performed for samples with sufficient DMI to promote the formation of Neel walls instead of Bloch configurations at rest, but two different magnitudes of the DMI were evaluated according to recent experimental measurements.[43] The μM results for a typical weak DMI structure (Ta-sample) are accurately described by the one-dimensional model (Rigid-1DM) just in terms of the DW position (X) and the internal DW angle (Φ), confirming the validity of this simple description due to the negligible tilting of the DW normal ($\chi \approx 0°$) for such weak DMI samples ($|D| \approx 0.05$ mJ/m^2). Approximate solutions for the terminal DW velocity were presented under in-plane fields for both the low-current (SHE-limited) and the high-current (DMI-limited) regimes, in good quantitative agreement with μM and 1DM numerical solutions.

When these μM and 1DM studies are carried out for a typical strong DMI Pt-sample ($|D| \approx 1.2$ mJ/m^2), the DW tilting plays a significant role to understand the current-induced DW dynamics. Our results indicate that in general a Tilt-1DM (X, Φ, χ), which describes the DW motion in terms also of the DW tilt angle χ, provides a better qualitative description of the full μM results than the Rigid-1DM (X, Φ). However, the agreement between both the Tilt-1DM and full μM is not completely satisfactory for all the range of analyzed in-plane fields. In particular, even for the low

current studied here, the increase of the DW velocity v for negative longitudinal fields $B_x < 0$ (along the inherent DW moment) cannot be quantitatively described by the Tilt-1DM, which similarly to the Rigid-1DM, also predicts a plateau of the DW velocity in the analyzed current and fields ranges. These discrepancies with μM simulations are related to the limitations of the Tilt-1DM, which assumes that all magnetic moments within the DW rotate uniformly, whereas μM results indicate that these moments exhibit some distribution of the rotation angles. Moreover, a DW in the Tilt-1DM acts as a rigid line when it tilts, whereas the micromagnetically accurate DW is not a rigid line and exhibits bowing in the tilting process. Also the variations of the DW width were demonstrated to play a significant role in understanding both micromagnetic and experimental results, in particular, when the longitudinal field is applied along the inherent DW moment imposed by strong DMI.

Finally, it was also verified that under realistic conditions including edge roughness and thermal activation, the DW tilting arises from strong DMI, confirming our interpretation of the experimental observations for the Pt/CoFe/MgO.[43] This study contributes to the understanding of the current-induced DW motion by the spin Hall effect along high perpendicular magnetocrystalline multilayers with DMI, and it suggests that a full micromagnetic modeling is required to achieve a better description of the experimental measurements for strong DMI samples, whereas a simple Rigid-1DM suffices to describe quantitatively the DW dynamics in weak-DMI samples. Our analysis is particularly relevant from a fundamental point of view. Nowadays, several experimental works are using the one-dimensional models to interpret their velocity measurements as a function of the longitudinal field, and the estimation of D is done from the field required to reverse the direction of the current-induced DW motion. Although this velocity-based method seems to be proper for weak-DMI samples ($|D| \sim 0.05$ mJ/m^2) it is not free of shortcomings. Indeed, the possible changes in the DW width, the incertitude on the damping, the details of the pinning, and the role of the Joule heating could provide poor estimations of D. The limitations of this velocity-based method are exacerbated for systems with strong DMI ($|D| \sim 1$ mJ/m^2), where the longitudinal fields required to reverse the DW chirality and current-driven DW motion direction could be large enough to promote the destabilization of the single-DW configuration with nucleation of multiple domains. From the technological point of view, strong DMI systems with high spin Hall angle and low damping are desirable to achieve high performance DW-based devices, with high DW velocities under low currents. On the other hand, strong DMI can give rise to significant DW tilting which limits the distance between adjacent walls, and consequently, the maximum density of the stored information.

ACKNOWLEDGMENTS

[1]D. Ravelosona, D. Lacour, J. A. Katine, B. D. Terris, and C. Chappert, Phys. Rev. Lett. **95**, 117203 (2005).

[2]W. W. Lin, H. Sang, D. Liu, Z. S. Jiang, A. Hu, and X. S. Wu, J. Appl. **99**, 08G518 (2006).

[3]O. Boulle, J. Kimling, P. Warnicke, M. Klaui, U. Rudinger, G. Malinowski, H. J. Swagten, B. Koopmans, C. Ulysse, and G. Faini, Phys. Rev. Lett. **101**, 216601 (2008).

[4]L. San Emeterio Alvarez, K.-Y. Wang, S. Lepadatu, S. Landi, S. J. Bending, and C. H. Marrows, Phys. Rev. Lett. **104**, 137205 (2010).

[5]I. M. Miron, T. Moore, H. Szambolics, L. D. Buda-Prejbeanu, S. Auffret, B. Rodmacq, S. Pizzini, J. Vogel, A. Bonfim, A. Schuhl, and G. Gaudin, Nature Mater. **10**, 419 (2011).

[6]P. P. J. Haazen, E. Mure, J. H. Franken, R. Lavrijsen, H. J. M. Swagten, and B. Koopmans, Nature Mater. **12**, 299 (2013).

[7]S. Emori, U. Bauer, S.-M. Ahn, E. Martinez, and G. S. D. Beach, Nature Mater. **12**, 611 (2013).

[8]K.-S. Ryu, L. Thomas, S.-H. Yang, and S. Parkin, Nat. Nanotechnol. **8**, 527 (2013).

[9]S. S. P. Parkin, M. Hayashi, and L. Thomas, Science **320**, 190 (2008).

[10]Yu. A. Bychkov and E. I. Rashba, JETP Lett. **39**, 78 (1984).

[11]A. Manchon and S. Zhang, Phys. Rev. B **78**, 212405 (2008); A. Manchon and S. Zhang, *ibid.* **79**, 094422 (2009).

[12]P. Gambardella and I. M. Miron, Philos. Trans. R. Soc. A **369**, 3175 (2011).

[13]K.-W. Kim, S.-M. Seo, J. Ryu, K.-J. Lee, and H.-W. Lee, Phys. Rev. B. **85**, 180404(R) (2012).

[14]X. Wang and A. Manchon. Phys. Rev. Lett. **108**, 117201 (2012).

[15]K.-W. Kim, H.-W. Lee, K.-J. Lee, and M. D. Stiles, Phys. Rev. Lett. **111**, 216601 (2013).

[16]S. Zhang and Z. Li, Phys. Rev. Lett. **93**, 127204 (2004).

[17]A. Thiaville, Y. Nakatani, J. Miltat, and Y. Suzuki, Europhys. Lett. **69**, 990 (2005).

[18]I. M. Miron, G. Gaudin, S. Auffret, B. Rodmacq, A. Schuhl, S. Pizzini, J. Vogel, and P. Gambardella, Nature Mater. **9**, 230 (2010).

[19]T. A. Moore, I. M. Miron, G. Gaudin, G. Serret, S. Auffret, B. Rodmacq, A. Schuhl, S. Pizzini, J. Vogel, and M. Bonfim, Appl. Phys. Lett. **93**, 262504 (2008).

[20]I. M. Miron, P.-J. Zermatten, G. Gaudin, S. Auffret, B. Rodmacq, and A. Schuhl, Phys. Rev. Lett. **102**, 137202 (2009).

[21]M. Cormier, A. Mougin, J. Ferre, A. Thiaville, N. Charpentier, F. Piechon, R. Weil, V. Baltz, and B. Rodmacq, Phys. Rev. B **81**, 024407 (2010).

[22]H. Tanigawa, T. Suzuki, S. Fukami, K. Suemitsu, N. Ohshima, and E. Kariyada, Appl. Phys. Lett. **102**, 152410 (2013).

[23]S. Emori and G. S. D. Beach, J. Phys.: Condens. Matter **24**, 024214 (2012).

[24]E. Martinez, L. Torres, and L. Lopez-Diaz, Phys. Rev. B **83**, 174444 (2011).

[25]A. V. Khvalkovskiy, V. Cros, D. Apalkov, V. Nikitin, M. Krounbi, K. A. Zvezdin, A. Anane, J. Grollier, and A. Fert, Phys. Rev. B **87**, 020402(R) (2013).

[26]M. Dyakonov and V. Perel, JETP Lett. **13**, 467 (1971).

[27]J. E. Hirsch, Phys. Rev. Lett. **83**, 1834 (1999).

[28]B. Gu, I. Sugai, T. Ziman, G. Y. Guo, N. Nagaosa, T. Seki, K. Takanashi, and S. Maekawa, Phys. Rev. Lett. **105**, 216401 (2010).

[29]L. Liu, T. Moriyama, D. C. Ralph, and R. A. Buhrman, Phys Rev. Lett. **106**, 036601 (2011).

[30]L. Liu, C.-F. Pai, Y. Li, H. W. Tseng, D. C. Ralph, and R. A. Buhrman, Science **336**, 555 (2012).

[31]K. Kondou, H. Sukegawa, S. Mitani, K. Tsukagoshi, and S. Kasai, Appl. Phys. Express **5**, 073002 (2012).

[32]S.-M. Seo, K.-W. Kim, J. Ryu, H.-W. Lee, and K.-J. Lee, Appl. Phys. Lett. **101**, 022405 (2012).

[33]A. Thiaville, S. Rohart, E. Jue, V. Cros, and A. Fert, Europhys. Lett. **100**, 57002 (2012).

[34]T. Moriya, Phys. Rev. Lett. **4**, 228 (1960).

[35]M. Bode, M. Heide, K. von Bergmann, P. Ferriani, S. Heinze, G. Bihlmayer, A. Kubetzka, O. Pietzsch, S. Blugel, and R. Wiesendanger, Nature **447**, 190 (2007).

[36]M. Heide, G. Bihlmayer, and S. Blugel, Phys. Rev. B **78**, 140403 (2008).

[37]X. Z. Yu, Y. Onose, N. Kanazawa, J. H. Park, J. H. Han, Y. Matsui, N. Nagaosa, and Y. Tokura, Nature **465**, 901 (2010).

[38]S. Heinze, K. von Bergmann, M. Menzel, J. Brede, A. Kubetzka, R. Wiesendanger, G. Bihlmayer, and S. Blugel, Nature Phys. **7**, 713 (2011).

[39]S. X. Huang and C. L. Chien, Phys. Rev. Lett. **108**, 267201 (2012).

[40]O. J. Lee, L. Q. Liu, C. F. Pai, Y. Li, H. W. Tseng, P. G. Gowtham, J. P. Park, D. C. Ralph, and R. A. Buhrman, Phys. Rev. B **89**, 024418 (2014).

[41]E. Martinez, S. Emori, and G. S. D. Beach, Appl. Phys. Lett. **103**, 072406 (2013).

[42]O. Boulle, S. Rohart, L. D. Buda-Prejbeanu, E. Jue, I. M. Miron, S. Pizzini, J. Vogel, G. Gaudin, and A. Thiaville, Phys. Rev. Lett. **111**, 217203 (2013).

[43]S. Emori, E. Martinez, U. Bauer, S.-M. Ahn, and G. S. D. Beach, "Spin Hall torque magnetometry of Dzyaloshinskii domain walls," e-print arXiv:1308.1432 (2013).

[44]S. Ikeda, K. Miura, H. Yamamoto, K. Mizunuma, H. D. Gan, M. Endo, S. Kanai, J. Hayakawa, F. Matsukura, and H. Ohno, Nature Mater. **9**, 721–724 (2010).

[45]S. Iihama, Q. Ma, T. Kubota, S. Mizukami, Y. Ando, and T. Miyazaki, Appl. Phys. Express **5**, 083001 (2012).

[46]A. J. Schellekens, L. Deen, D. Wang, J. T. Kohlhepp, H. J. M. Swagten, and B. Koopmans, Appl. Phys. Lett. **102**, 082405 (2013).

[47]G. Bertotti, *Hysteresis in Magnetism: For Physicists, Materials Scientists and Engineers* (Acad. Press, San Diego, California, 1998).

[48]S. Rohart and A. Thiaville, Phys. Rev. B **88**, 184422 (2013).

[49]X. Fan, J. Wu, Y. Chen, M. J. Jerry, H. Zhang, and J. Q. Xiao, Nat. Commun. **4**, 1799 (2013).

[50]X. Fan, H. Celik, J. Wu, C. Ni, K.-J. Lee, V. O. Lorenz, and J. Q. Xiao. Nat. Commun. **5**, 3042 (2014).

[51]C.-F. Pai, M.-H. Nguyen, C. Belvin, L. H. Vilela-Leo, D. C. Ralph, and R. A. Buhrman, Appl. Phys. Lett. **104**, 082407 (2014).

[52]E. Martinez and G. Finocchio, IEEE Trans. Magn. **49**(7), 3105 (2013).

[53]E. Martinez, G. Finocchio, L. Torres, and L. Lopez-Diaz, AIP Adv. **3**, 072109 (2013).

[54]See http://www.goparallel.net/index.php/en/gp-software.html for details about the GPMagnet.

[55]L. Lopez-Diaz, D. Aurelio, L. Torres, E. Martinez, M. A. Hernandez-Lopez, J. Gomez, O. Alejos, M. Carpentieri, G. Finocchio, and G. Consolo, J. Phys. Appl. Phys. **45**, 323001 (2012).

[56]K.-S. Ryu, L. Thomas, S.-H. Yang, and S. S. P. Parkin, Appl. Phys. Express **5**, 093006 (2012).

[57]N. L. Schryer and L. R. Walker, J. Appl. Phys. **45**, 5406–5421 (1974).

[58]A. P. Malozemoff and J. C. Slonczewski, *Magnetic Domain Walls in Bubble Material* (Academic Press, 1979).

[59]E. Martinez, Adv. Condens. Matter Phys. **2012**, 954196 (2012).

[60]M. Hayashi, Y. Nakatani, S. Fukami, M. Yamanouchi, S. Mitani, and H. Ohno, J. Phys.: Condens. Matter **24**, 024221 (2012).

[61]O. Boulle, L. D. Buda-Prejbeanu, M. Miron, and G. Gaudin, J. Appl. Phys. **112**, 053901 (2012).

[62]P.-B. He, Z.-D. Zhou, R.-X. Wang, Z.-D. Li, M.-Q. Cai, and A.-L. Pan, J. Appl. Phys. **114**, 093912 (2013).

[63]L. Thomas, M. Hayashi, X. Jiang, R. Moriya, C. Rettner, and S. Parkin, Science **315**, 1553 (2007).

[64]E. Martinez, L. Lopez-Diaz, L. Torres, C. Tristan, and O. Alejos, Phys. Rev. B **75**, 174409 (2007).

[65]E. Martinez, L. Lopez-Diaz, O. Alejos, L. Torres, and C. Tristan, Phys. Rev. Lett. **98**, 267202 (2007).

[66]R. A. Duine, A. S. Nunez, and A. H. MacDonald, Phys. Rev. Lett. **98**, 056605 (2007).

[67]E. Martinez, L. Lopez-Diaz, O. Alejos, and L. Torres, J. Appl. Phys. **106**, 043914 (2009).

[68]E. Martinez, J. Phys.: Condens. Matter **24**, 024206 (2012).

[69]S. V. Tarasenko, A. Stankiewicz, V. V. Tarasenko, and J. Ferre, J. Magn. Magn. Mater. **189**, 19 (1998).

[70]Taking into account the analyzed dimensions and materials parameters of the Ta-sample, $H_D \approx -7.5\text{kA/m}$ and $H_K \approx 12.2\text{kA/m}$, so the approach $|H_D + H_x| \gg H_K$ does not fulfill. When $|H_D + H_x|$ is of the same order of magnitude as H_K, the analytical expressions (20), (21), and (22) require corrections, and v_T has therefore to be computed numerically from Eqs. (15) and (16). In spite of this, it was verified that the analytical expressions (20), (21), and (22) predict in a excellent manner the numerical results of Fig. 7.

[71]N. Perez, E. Martinez, L. Torres, S.-H. Woo, S. Emori, and G. S. D. Beach, Appl. Phys. Lett. **104**, 092403 (2014).

[72]The effect of the same edge roughness and thermal fluctuations at $T = 300\text{K}$ on both the field- and current-induced DW motion was also studied for the Ta sample. In this weak DMI case, no evidence of DW tilting was found considering these realistic conditions.